RSC Advances

PAPER

View Article Online
View Journal | View Issue

Cite this: *RSC Adv.*, 2026, **16**, 23190

Mechanosynthesis of a bismuth nanoparticle-decorated palm kernel mesocarp fiber (Bi-PKMF): adsorption of Pb(II), kinetics and thermodynamics

Amarachi Udoka Nkwoada, *[a] Simeon Chukwudozie Nwanonenyi, [b] Callistus Izunna Iheme, [c] Ali Bilar, [a] Ijeoma Akunna Duru, [a] Tochukwu Ifeanyi Nwakile, [a] Divinefavour Anioke, [a] Janefrances Oluebube Onwuemeodo, [a] Chukwuemeka Fortunatus Nnadozie, [a] Celestine Chidubem Chukwunonyerem, [a] Favour Ogadinma Izuagba [a] and Uchenna Gift Nwaneri [a]

A new bismuth-decorated palm kernel mesocarp fiber (Bi-PKMF) adsorbent was prepared through green liquid-assisted mechano-chemical grinding, followed by thermal crystallization. Detailed characterization (SEM-EDX, TEM, BET, FTIR, and AFM) was performed to verify the uniform dispersion of bismuth oxide nanoparticles in the lignocellulosic matrix and the production of a high-surface-area mesoporous material (387 $m^2\ g^{-1}$ and a pore size of 12.5 nm). Control experiments of the ball-milled PKMF indicated that bismuth functionalization provides chemical enhancement rather than mechanical enhancement. Bi-PKMF exhibited excellent Pb(II) adsorption capacity (112.3 mg g^{-1}), which was 231 times higher than that of pristine PKMF (48.5 mg g^{-1}) with more than 90% removal in 60 min at pH 6. The kinetics followed the pseudo-second-order model (R^2 = 0.999), and the obtained Dubinin–Radushkevich adsorption energy (12.6 kJ mol^{-1}) confirmed chemisorption. The mesoporous structure reduces the resistance to intraparticle diffusion, allowing access to the active sites (Bi–O, –OH, and –COO–). Spontaneous ($\Delta G° < 0$), exothermic ($\Delta H° = -29.02$ kJ mol^{-1}), and ordered adsorption were indicated by the thermodynamic parameters. The reusability of Bi-PKMF was good, retaining over 90% of its adsorption capacity after five regeneration cycles. The key to the increased Pb(II) uptake is surface chemistry, rather than physical structure, which makes Bi-PKMF a high-performance biosorbent for sustainable water purification.

Received 7th February 2026
Accepted 14th April 2026

DOI: 10.1039/d6ra01094f

rsc.li/rsc-advances

1 Introduction

One of the most urgent environmental issues of the twenty-first century is water quality degradation by heavy metals, particularly mercury (Hg), arsenic (As), cadmium (Cd), and lead (Pb).[1,2] These industrial effluent, mining, and agricultural runoff toxicants disrupt aquatic ecosystems and bioaccumulate in the food chain, ultimately threatening human health through dermal contact, ingestion, and inhalation.[3] New developments in the treatment of wastewater have seen a paradigm shift from traditional adsorbents towards novel functionalized biosorbents and nanoparticle-modified materials, such as polystyrene/periwinkle shells,[4] zeolite/periwinkle shells,[5] bismuth-based materials,[6] and functionalized palm kernel fruit fibers and palm kernel shell fibers,[7] as innovative and functionalized biosorbents and nanoparticle-decorated materials.

Among the heavy metals, lead (Pb(II)) is especially toxic, has no known biological role, and causes harmful effects even at minute concentrations. Epidemiological studies have proven that blood lead levels (BLLs) of 5 μg dL^{-1} in children are linked with reduced intelligence quotient, neurodevelopmental impairment, and behavioural disorders, while chronic exposure to lead in adulthood is related to hypertension, kidney dysfunction, and reproductive toxicity.[8] Importantly the U.S. Centers for Disease Control and Prevention (CDC) claims that there is no safe BLL; the neurological effects are evident at 5.0 g dL^{-1}.[9] Lead concentrations exceeding 400 mg kg^{-1} in contaminated soils can cause up to 42% root growth retardation[10] and pose long-term hazards through food chain transfer and ecosystem degradation; thus, there is an urgent need to develop effective lead remediation techniques.[11]

The palm oil industry also produces large amounts of lignocellulosic biomass waste, especially the palm kernel shell (PKS) and palm kernel mesocarp fiber (PKMF). These

[a]Department of Chemistry, Federal University of Technology, Owerri, Nigeria. E-mail: amarachi.nkwoada@futo.edu.ng
[b]Department of Polymer and Textile Engineering, Federal University of Technology, Owerri, Nigeria
[c]Department of Biochemistry, Federal University of Technology, Owerri, Nigeria

substances are commonly underused or burnt in the air, which leads to greenhouse gas emissions and particulate pollution.[12] Recent studies have demonstrated that PKS and PKMF can be employed as inexpensive biosorbents to remove heavy metals because they possess abundant active functional groups (hydroxyl, carboxyl, and phenolic) on their surfaces.[13,14] Under optimized conditions, unmodified PKS exhibits Pb(II) adsorption capacities of about 43.12 mg g^{-1} and removal efficiencies over 99%.[15] Further functionalization assists chemical removal; for example, sulfonation can remove about 95% of Pb(II) by improving surface chemistry and increasing the active-site density.[14] Despite these developments, the following severe constraints still remain: heterogeneous surface chemistry, inadequate nanoscale active sites, and absence of integrated surface-active agents in lignocellulosic matrices.[16,17] These deficiencies limit the performance in complicated wastewater matrices where several pollutants are present. Moreover, the majority of the current literature is devoted to the use of oil palm waste derivatives as palm kernel shell activated carbon,[16] biocatalysts,[18] and modified PKS adsorbents[19,20] without addressing these critical challenges. Thus, in this work, we made a direct attempt to investigate the synthesis of functionalized materials from palm kernel mesocarp fiber (PKMF) using bismuth for Pb(II) removal.

This is due to the ability of bismuth (Bi) to form a wide range of interfacial bonds, provide a large surface area, and create defect sites in adsorbent materials as a result of nano-bismuth oxide (Bi–O) doping and incorporation into heterostructures.[21] Nanomaterials made of bismuth have emerged as promising environmental remediation agents due to their distinct physicochemical characteristics, including low toxicity, high chemical stability, and affinity to heavy metal oxyanions and cations.[22] Bismuth-doped nanocomposites exhibit improved adsorption rates due to the synergistic nature of the adsorption process, namely surface complexation, ion exchange, and electrostatic interaction. An example is the use of bismuth-impregnated sludge-derived biochar, which showed a high uranium(VI) adsorption capacity (516.5 mg g^{-1} and 93.8% removal) through the affinity of bismuth towards oxyanions, which was 21 times higher compared to undoped biochar (average capacity of 100–300 mg g^{-1}).[23] Similarly, bismuth-doped metal oxides (PBCuO) have been found to exhibit excellent activity for the photocatalytic degradation (93.10%) of organic pollutants owing to their low band gaps (2.43 eV) and larger surface areas (88.90 m^2 g^{-1}).[24] These achievements indicate that the incorporation of bismuth species in PKMF matrices is likely to overcome the drawbacks of pure biosorbents, producing hybrid products that possess enhanced adsorptive capacity. Therefore, herein, we present the synthesis of nanoparticle bismuth-doped palm kernel mesocarp fiber (PKMF) *via* mechano-synthesis, which enables uniform doping, nanoscale integration, and improved interfacial properties to remove Pb(II).

Traditional techniques for producing nanocomposites (hydrothermal and sol–gel) normally require high temperatures (>200 °C), long reaction times, and toxic solvents, which are incompatible with the concept of green chemistry.[25] Alternatively, mechanochemical synthesis, especially liquid-assisted grinding (LAG), is another promising option because it uses mechanical energy to induce solid–state reactions at ambient temperature with low solvent concentrations (η < 1–2 μL mg^{-1}).[26] This facilitates the homogenous integration of bismuth species in biomass. The obtained materials possess enhanced surface areas, designed porosity, and high concentration of active sites, qualities that are vital in effective Pb(II) sequestration. Furthermore, LAG mechano-synthesis can be economically scaled, is environmentally friendly, and can be applied to agricultural waste, aligning with the principles of a circular economy while producing materials with nanoscale dispersion without aggregation or disruption of the lignocellulosic structure.[27]

Although palm kernel shell adsorbents and bismuth-based materials have been studied extensively as individual adsorbents, no reported study employed bismuth-functionalized palm kernel mesocarp fiber in the removal of Pb(II), which has been a significant missed opportunity to capitalize on the low-cost nature of the PKMF with the high adsorption capability of bismuth nanoparticles through green mechanochemical synthesis. In response to this omission, the current study was guided by the following questions: can bismuth oxide nanoparticles be selectively functionalised on PKMF *via* a solution-minimised mechanochemical-thermal process? How would bismuth functionalisation affect the physicochemical properties of PKMF? Would the adsorption capacity of Bi-PKMF be enhanced compared with that of pristine PKMF? How would the operating parameters affect its performance? Which kinetic, isotherm, and thermodynamic models best describe the adsorption process? What drives the mechanism, and would Bi-PKMF be regenerable for multiple adsorption–desorption cycles[28]? To this end, the detailed aims of this study were to synthesize Bi-PKMF *via* liquid-assisted mechanochemical grinding and subsequent thermal crystallization, to thoroughly characterize it using the SEM-EDX, TEM, XRD, AFM, FTIR, and BET techniques, to evaluate its performance for Pb(II) adsorption under varying conditions, to model its adsorption kinetics, isotherms, and thermodynamics, and to assess its reusability. Bi-PKMF was found to be an excellent adsorbent for the removal of heavy metal ions from water, requiring a very short time of only 1 h to remove Pb(II), with a removal efficiency of ≥90.02% compared with that of ≤85.01% for PKMF.

2 Materials and methods

2.1 Chemicals and reagents

Elaeis guineensis (palm kernel) is derived from the oil palm tree and was sourced from a local oil mill in Orlu, Imo State, Nigeria. Analytical grade bismuth(II) nitrate pentahydrate ($Bi(NO_3)_3 \cdot 5H_20$, 98%, CAS no. 10035-06-0) and lead nitrate ($Pb(NO_3)_2$, 98%, CAS: 10099-74-8) were supplied by Gate Lab Chemicals Ltd and were used as received without further purification. A stock solution of Pb^{2+} (1000 mg L^{-1}) was formulated by dissolving 1.598 g of $Pb(NO_3)_2$ in a small amount of deionized water (DI water, resistivity 18.2 MΩ cm) with the addition of 1 mL of concentrated HNO_3 to inhibit hydrolysis and make the solution stable. It was

then transferred to a volumetric flask and quantitatively diluted to 1000 mL with deionized water. Serial dilution of the stock solution using DI water was used to prepare working solutions of desired concentrations, which were prepared daily to ensure accuracy and limit degradation. The pH of the solution was kept at 7.0 by adding 0.1 M HCl or 0.1 M NaOH accordingly. All solutions were made in DI water, and glassware was thoroughly rinsed with deionized water before use.

2.2 Palm kernel mesocarp fiber (PKSF) preparation

300 g of palm kernel mesocarp fiber (PKMF) was collected from a local oil mill after red palm oil was completely extracted from the mesocarp, and the material was sundried for 6 h a day over 3 continuous days at temperatures ≥28 °C.[29,30] The palm kernel mesocarp fiber was dried in the sun, then solvent-extracted in ethanol with a 1 : 10 solid-to-solvent ratio, and stirred at 50–60 °C to extract the remaining oils. The fiber was recovered by filtration, and further washing with hot deionized water at 80–90 °C was repeated to remove traces of the solvent and any water-soluble impurities in the filtrate until a clear filtrate was obtained. The palm kernel mesocarp fiber (PKMF) was dried in an oven at 105 °C to a constant weight of 267.5 g and placed in a desiccator before proceeding to the preparation of the nano-adsorbent. The PKMF was manually cut with sanitized scissors to 1–2 cm and then milled using an IKA MF 10 basic grinder with a 2 mm sieve to a size of ≤250 μm.

2.3 Synthesis of the bismuth-decorated palm kernel mesocarp fiber (Bi-PKMF)

The functionalization of the palm kernel mesocarp fiber (PKMF) was carried out through a two-step mechanochemical-thermal process on the cleaned and milled fibers.

2.3.1 Step 1: liquid-assisted mechanochemical synthesis. 10.0 g of dried PKMF (particle size: 150–250 μm) was milled in a 500 mL zirconia milling jar. A solution of bismuth nitrate pentahydrate ($Bi(NO_3)_3 \cdot 5H_2O$) in water was prepared as the doping precursor. To achieve a successful mechanochemical reaction and retain a paste-like consistency that can be used in grinding, a liquid-to-solid ratio (η) of 0.5 μL mg^{-1} was applied.[31] Thus, 5.0 mL of a 1.0 M solution of $Bi(NO_3)_3 \cdot 5H_2O$ was added to the jar, and a nominal loading of 10 wt% of Bi was obtained with respect to the PKMF. Then, 20 zirconia grinding balls (10 mm diameter) were added, and the mass ratio of balls to powder was 20 : 1. The mixture was mixed in a planetary ball mill (Retsch PM 100) at 350 rpm over a period of 4 h. This is a high-energy reaction necessary to physically mix, reduce the particle size, and chemically initiate the interaction between the bismuth precursor and the fibrous substrate, forming a slurry.[32]

2.3.2 Step 2: thermal crystallization. The product from mechanochemical synthesis was collected as the resulting slurry and quantitatively transferred to a 100 mL Teflon-lined stainless-steel autoclave (Model KH-100, Yanzheng Instrument, China). The wet reaction mixture (15–20 mL of slurry with 10.5 g of equivalent dry mass) was added to the autoclave to fill it to a total volume of about 15–20%, with enough headspace to allow the safe development of pressure during heating. The autoclave was placed in a convection oven at 120 °C and incubated over a period of 6 h. The hydrothermal process helps in the full thermal decomposition of the bismuth nitrate starting material, crystallization of the bismuth oxide (Bi_2O_3) nanoparticles, and their immobilization to the PKMF substrate.[33,34] Under these circumstances, the organic components (*e.g.* lignin and cellulose) of the PKMF can serve as mild reducing agents and stabilizing compounds.[30] The composite was then cooled and collected by vacuum filtration, followed by washing with deionized water and ethanol to remove the unreacted ions, and then drying overnight at 80 °C in a laboratory oven. The end-product is denoted as bismuth-PKMF (Bi-PKMF).

2.4 Materials and analytical methods

2.4.1 Morphological and elemental analysis (SEM-EDX). Scanning electron microscopy (SEM) with energy-dispersive X-ray spectroscopy (EDX) was used to study the surface morphology and elemental composition of Bi-PKMF. Before imaging, the samples were delicately fixed on aluminium stubs and sputter-coated with approximately 20 nm of carbon on their surface using a QUORUM Q150R ES sputter coater to reduce surface charging and enhance the image quality. SEM was performed on a Phenom ProX SEM, which had an Oxford Instruments XMax 50 silicon drift detector (SDD). Micrographs and EDX spectra were obtained under high vacuum at an accelerating voltage of 15 kV. Several areas of each sample were examined to achieve representative morphological analysis, and elemental analysis was carried out using the standardless ZAF correction of the instrument. EDX analysis was performed on five randomly selected regions per sample, and the results are reported as mean ± standard deviation to ensure a representative compositional assessment.

2.4.2 Transmission electron microscopy (TEM). High-resolution transmission electron microscopy (HR-TEM) on a JEM-ARM200F-G microscope was performed to examine internal nanostructure, particle dispersion, and size distribution. For TEM analysis, a certain amount of the Bi-PKMF sample was dispersed in methanol and ultrasonicated for 45 min to achieve sufficient de-aggregation. The resulting suspension was then carefully placed on a carbon-coated copper grid (300 mesh) and left to dry under ambient conditions before analysis. Imaging was performed at an accelerating voltage suitable for visualizing high-resolution lattice images, allowing for detailed observation of nanoscale images and interactions between particles and the matrix.

2.4.3 Crystalline phase identification (XRD). Powder X-ray diffraction (XRD) was performed on a Thermo Scientific ARL X'TRA diffractometer using Cu Kα radiation (1.5406 Å) with a nickel filter to determine the crystalline structure and phase composition of Bi-PKMF. Diffraction patterns were recorded with 50 scans in a continuous scan mode over the 2θ range of 5–90°. Phase identification was carried out by comparing the experimental diffraction patterns with reference data from the International Centre of Diffraction Data (ICDD) database. The sample was packed in a stable manner to minimize preferred orientation effects.

2.4.4 Surface topography analysis (AFM). The topography of the surfaces, as well as their nanoscale roughness, were measured using an atomic force microscope (AFM; Park Systems XE-70) in tapping mode to avoid damaging the surfaces. Measurements were performed under ambient conditions, and scans were conducted in various random regions to ensure that they were statistically representative. The images were then analyzed using the manufacturer's software to obtain qualitative and quantitative roughness parameters of the surfaces.

2.4.5 Functional group and bonding analysis (FTIR). Fourier transform infrared (FTIR) spectroscopy was used to identify the surface functional groups and chemical bonding environment of Bi-PKMF using a PerkinElmer Spectrum Two spectrometer with a mid-infrared triglycine sulfate (MIR-TGS) detector. 1 mg of the composite was mixed homogeneously with 100 mg of anhydrous KBr and then subjected to pellet formation through the use of hydraulic pressure. Spectra were recorded in the range of 4000–400 cm^{-1} at a resolution of 4 cm^{-1}, and repeated scans were averaged to improve the signal-to-noise ratio.

2.4.6 Textural properties and surface area study (BET). Nitrogen adsorption–desorption isotherms were measured at 77 K, and the specific surface area, pore volume, and pore size distribution were determined using a Quantachrome NOVA-Touch Series analyzer (Anton Paar). The samples were pre-treated by vacuum drying at 150 °C over a period of 12 h before analysis to eliminate physically adsorbed moisture and gases. The Brunauer–Emmett–Teller (BET) method was used to calculate the specific surface area within the appropriate relative pressure range. The total pore volume was determined using the amount of nitrogen adsorbed at P/P_0 of 0.99. The *t*-plot method was used to assess micropore surface area and volume, while the desorption branch of the isotherm was used to estimate mesopore size distribution using the Barrett–Joyner–Halenda (BJH) model.

2.5 Adsorption experiments

The amount of aqueous Pb(II) ions in the adsorption experiments was determined by atomic absorption spectroscopy (AAS) on a PinAAcle 900F spectrometer (PerkinElmer Inc., USA). The samples were analyzed using instrument calibration with freshly prepared Pb(II) standard solutions in the concentration range of 10–100 mg L^{-1} to provide a calibration curve with a correlation coefficient (R^2) greater than 0.999. All measurements were repeated three times and, to ensure the reliability of the analysis, procedural blanks were measured and compared to the samples to confirm that there was no contamination.

2.5.1 Adsorption properties of Bi-PKMF and PKMF. The following equations were used to calculate the quantity of each metal adsorbed (q_e) and the percentage removal (R%) in all the experiments.

$$q_e = (C_0 - C_e)V/m \quad (1)$$

$$R\% = \frac{C_0 - C_e}{C_0} \times 100 \quad (2)$$

where C_0 and C_e are the initial and equilibrium concentrations of metal (mg L^{-1}), and V and m are the volume of aqueous metal solution (L) and the dosage of adsorbent (g), respectively. All experiments were performed in triplicate and the average was used as the experimental data.

2.5.2 pH effect. The pH of a solution plays a significant role in adsorption studies because it impacts adsorbate solubility, the concentration of metal ions, and the charge of the functional groups in the adsorbent. Specifically, 0.1 g of PKMF or Bi-PKMF was added to a metal solution (50 mg L^{-1} Pb) in an Erlenmeyer flask (50 mL), adjusted to various pH levels (2, 4, 5, 6, 7, 8, and 10) and shaken on a shaker for 2 h. Then, the solution mixture was filtered, and the Pb(II) concentration in the filtrate was measured using an atomic absorption spectrophotometer.

2.5.3 Adsorbent dosage. Adsorbent dosage is known to have a tremendous influence on the entire adsorption process. To study the effects of various doses of PKMF and Bi-PKMF on the adsorption efficiency of Pb(II) ions, different doses of PKMF and Bi-PKMF (0.05, 0.1, 0.2, 0.3, 0.5, and 1.0 g) were added to 50 mL of Pb(II) solution (50 mg L^{-1}) with a constant pH of 6. An atomic absorption spectrophotometer was used to determine the lead concentration in the filtrate.

2.5.4 Initial concentration. The initial concentration of the adsorbate also impacts the adsorption process, and thus, it was investigated. 50 mL solutions with different concentrations of Pb(II) (10, 20, 30, 50, 75, and 100 mg L^{-1}) were mixed with 0.3 g, as the optimized dosage, of PKMF or Bi-PKMF at pH 6, and left to equilibrate at 25 °C for 2 h. The concentration of Pb(II) remaining in the filtrate was measured using an atomic absorption spectrophotometer. The equilibrium data obtained from this initial concentration study were subsequently used for adsorption isotherm modelling.

2.5.5 Contact time. Significant parameters associated with equilibrium time indicate that the metal removal time needs to be optimized during the adsorption process. 0.3 g (optimized dosage) of PKMF or Bi-PKMF was combined with 50 mL of Pb(II) solution (50 mg L^{-1}) at pH 6 and solution temperature of 25 °C for intervals of 30, 60, 120, and 180 min. At fixed intervals, the concentration of Pb(II) in the filtrate was measured using an atomic absorption spectrophotometer.

2.5.6 Temperature effect. The influence of adsorption temperature was studied at solution temperatures of 25 °C, 35 °C, 45 °C, and 55 °C while keeping all the above-mentioned equilibrium parameters constant. The solution was filtered, and the concentration of Pb(II) in the filtrate was measured using an atomic absorption spectrophotometer.

3 Results and discussion

3.1 Bi-PKMF characterization

3.1.1 SEM-EDX result. The SEM-EDX analysis (Fig. 1) confirms the successful synthesis of thebismuth nanoparticle-decorated palm kernel mesocarp fiber (Bi-PKMF). The EDX analysis (Fig. 1a) shows that the bismuth (Bi) content is high (13.4 wt%), directly indicating the successful integration of bismuth species into the lignocellulosic fiber matrix.[23] The

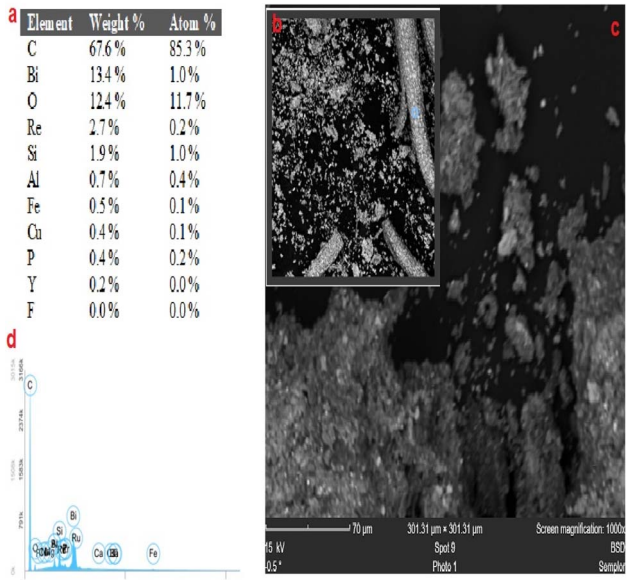

Fig. 1 Morphological and elemental characterization of Bi-PKMF: (a) EDX quantitative analysis, (b) SEM micrograph of Bi-PKMF fiber morphology, (c) higher-magnification SEM image showing surface texture, and (d) representative EDX spectrum confirming elemental composition. N/B: trace rhenium (Re) signals in EDX spectra arise from the Re-W sputter coating target used for sample preparation and are not intrinsic to the Bi-PKMF material.

corresponding spectrum and elemental mapping (Fig. 1a–d) exhibit a uniform distribution of Bi, which implies that the liquid-assisted mechanochemical reaction is effective in preventing the aggregation of the nanoparticles and facilitating interfacial bonding. The SEM micrographs (Fig. 1b and c) show the typical fibrous structure of PKMF, and functionalization with the bismuth-based nanoparticles led to an increase in surface area and the formation of new adsorption sites. This structural alteration is important because the introduced bismuth oxide nanoparticles are reported to have an affinity to heavy metal cations, such as Pb(II), due to enhanced surface complexation and ion-exchange processes.[22] Other constituents such as Si, Al, and Fe are trace elements that are usually present in agro-waste biomass. This selective functionalization of bismuth distinguishes Bi-PKMF from pristine PKMF. This design results in a high adsorption capacity and rate, a phenomenon also observed with other bismuth-decorated biosorbents.[23]

In addition, the elemental composition of the pristine PKMF and Bi-PKMF was measured using energy-dispersive X-ray spectroscopy at five randomly chosen locations on each sample to ensure representative and statistically significant results. The elemental compositions of both samples are presented in the form of mean values with standard deviations to reflect the homogeneity of the elemental distribution across the surfaces of the samples. As shown in Table 1, pristine PKMF is dominated by 58.7 ± 2.8 wt% and 38.2 ± 2.1 wt% of carbon and oxygen, respectively, which is typical of lignocellulosic biomass, with trace amounts of naturally occurring mineral elements,

Table 1 Multi-spot analysis to determine average composition. Average elemental composition of pristine PKMF obtained from multi-spot EDX analysis ($n = 5$)[a]

Element	Weight% (mean ± SD)	Atomic% (mean ± SD)
Carbon (C)	59.1 ± 2.7	67.5 ± 2.5
Oxygen (O)	38.5 ± 2.0	33.0 ± 1.8
Silicon (Si)	1.6 ± 0.4	0.8 ± 0.2
Aluminium (Al)	0.8 ± 0.3	0.4 ± 0.2
Potassium (K)	0.4 ± 0.2	0.1 ± 0.1
Calcium (Ca)	0.3 ± 0.1	0.1 ± 0.1

[a] Rhenium (Re) signals (originally ~0.7 wt%) arising from the sputter coating were excluded from these calculations; values are normalized to Re-free composition.

such as silicon, aluminium, potassium, and calcium, introduced into the biomass during the growth and processing of palm kernels. After mechanochemical bismuth functionalization, as shown in Table 2, Bi-PKMF still contained carbon and oxygen as its main components with contents of 52.4 ± 3.2 wt% and 31.8 ± 2.5 wt%, respectively, while the bismuth content of 12.6 ± 1.8 wt% is relatively high and uniformly distributed across the Bi-PKMF structure. This also confirms the successful homogeneous distribution of bismuth species across the fiber structure based on TEM and EDX mapping analysis. The minor decrease in the weight percentage of carbon and oxygen in Bi-PKMF relative to pristine PKMF is due to the dilution effect caused by the addition of bismuth in the lignocellulosic structure. It is important to note that the trace rhenium signals detected in both samples, with contents of about 0.7–0.8 wt%, are artefacts resulting from the rhenium-tungsten sputter coating target used in the preparation of the SEM samples to increase their conductivity, and thus do not reflect the elemental components in the adsorbent materials. The overall elemental analysis verifies that PKMF was successfully functionalized with bismuth, and that compositional reproducibility was achieved using the liquid-assisted mechanochemical synthesis methodology.

3.1.2 TEM results. The TEM images provide important nanoscale information about the effective design of the nanoparticle-decorated Bi-PKMF. The bismuth nanoparticles appear as dense, high-contrast features, while the fiber matrix

Table 2 Multi-spot analysis to determine average composition. Average elemental composition of Bi-PKMF obtained from multi-spot EDX analysis ($n = 5$)[a]

Element	Weight% (mean ± SD)	Atomic% (mean ± SD)
Carbon (C)	52.8 ± 3.1	65.1 ± 2.8
Oxygen (O)	32.1 ± 2.4	29.7 ± 2.0
Bismuth (Bi)	12.7 ± 1.7	3.2 ± 0.5
Silicon (Si)	1.8 ± 0.4	1.0 ± 0.2
Aluminium (Al)	0.9 ± 0.3	0.5 ± 0.2
Calcium (Ca)	0.5 ± 0.2	0.2 ± 0.1

[a] Rhenium (Re) signals (originally ~0.8 wt%) arising from the sputter coating were excluded from these calculations; values are normalized to Re-free composition.

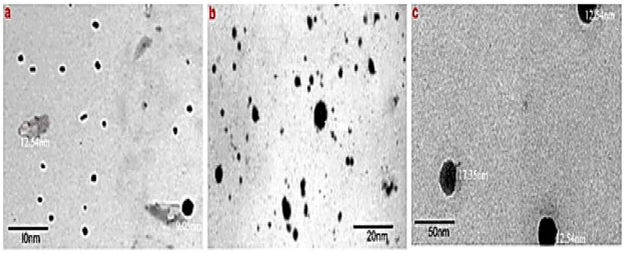

Fig. 2 Nanostructural analysis of Bi-PKMF. Transmission electron microscopy (TEM) micrographs showing the dispersion of bismuth oxide nanoparticles (dark phases) on the palm kernel mesocarp fiber matrix at increasing magnifications: (a) 10 nm scale bar, (b) 20 nm scale bar, and (c) 50 nm scale bar. The images illustrate the distribution and size variation of Bi_2O_3 nanoparticles within the fibrous matrix.

remains subtly visible as a diffuse, electron-transparent background.

This contrast arises from the substantial difference in electron density between the high-atomic-number bismuth ($Z = 83$) and the low-atomic-number constituents (carbon, oxygen, and hydrogen) in the lignocellulosic biomass. The micrographs display the bismuth-based nanoparticles, where the sizes are about 10 to 50 nm in diameter and uniformly distributed and attached to the fibrous palm kernel mesocarp matrix. This confirms the effectiveness of the mechanochemical and thermal synthesis in the realization of nanoscale integration with minimal aggregation, which is typical of biomass-based composites. The proximity of the high-aspect-ratio particles to the fiber substrate reduces the interfacial resistance, thereby maximizing the available active sites.[22] Although some micron-scale agglomerates are visible in the SEM images (likely due to drying), high-resolution TEM confirms that the size of the primary bismuth oxide nanoparticles remains in the 10–50 nm range and they are uniformly distributed on the nanoscale.

Nanostructures are conducive to the adsorption kinetics because the small particle size reduces the internal diffusion barriers to Pb(II) ions and thus enables surface complexation of these ions within a short time. The suggested large surface area and clearly exposed bismuth oxide phases are associated with the predicted excellent adsorption ability, as similar nanostructuring of bismuth-decorated biochar has been demonstrated to increase the rapid uptake of pollutants.[35] This engineered nanodispersion is a key structural feature that explains the superior removal performance of Bi-PKMF compared with the pristine fiber or micron-scale composites.[36]

Furthermore, to validate the incorporation of bismuth into the palm kernel mesocarp fibers, as observed by SEM and TEM analyses, energy-dispersive X-ray (EDX) elemental mapping was conducted, as shown in Fig. 3. The representative SEM image of Bi-PKMF (Fig. 3a) illustrates a fibrous morphology, with visible bismuth-containing nanoparticles (lighter-contrast regions) decorating the surface.

This morphology is typical of the regions analysed by EDX mapping (Fig. 3a–e), confirming that the bismuth distribution shown in the maps corresponds to the fiber substrate rather than isolated agglomerates. The EDX elemental mapping

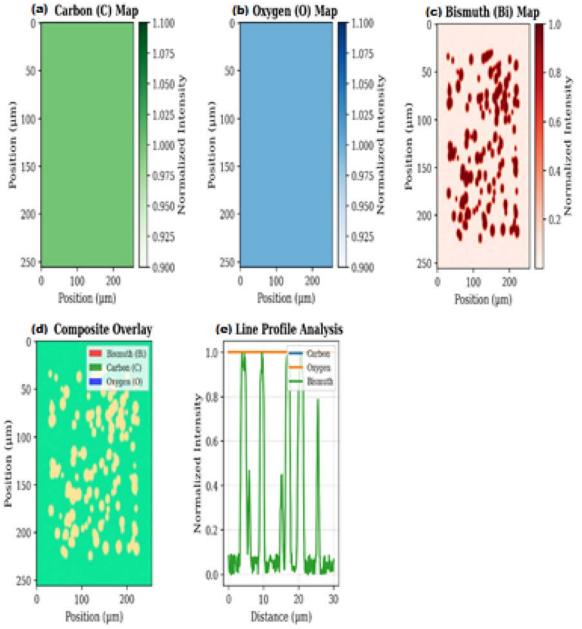

Fig. 3 Morphological and elemental characterization of Bi-PKMF: (a) carbon Kα1 elemental map, (b) oxygen Kα1 elemental map, (c) bismuth Mα1 elemental map, (d) composite overlay of all elements, and (e) line profile analysis. Note: the elemental maps in (a–e) were acquired from a region with identical morphology, confirming that bismuth nanoparticles are uniformly dispersed on the fiber surfaces.

presents convincing and straightforward visual evidence of the effective and uniform incorporation of bismuth into the palm kernel mesocarp fiber structure, confirming the synthesis and innovative structure of this material. The individual elemental maps clearly show the distribution of carbon and oxygen throughout the fibrous structure, which is characteristic of lignocellulosic biomass, whereas the bismuth map (Fig. 3c) clearly shows uniformly distributed red hotspots that are characteristic of the decorated nanoparticles. Importantly, the composite overlay (Fig. 3d) indicates a consistent combination in which bismuth signals (yellow) are closely entangled with the carbonaceous fiber structure (green), and there is no evidence of macroscopic phase separation. Quantitative line profile analysis (Fig. 3e) was performed across the composite overlay to assess the spatial correlation between bismuth and the fiber matrix. The overlapping Bi, C and O peaks along the transect confirm that the bismuth-containing nanoparticles are not merely deposited on the surface but are intimately embedded within the lignocellulosic framework, consistent with the TEM observations.

This co-localization was determined using the line profile analysis, which gives a quantitative measure by revealing areas of high carbon and oxygen content through simultaneous peaks in bismuth intensity. This spatial correlation directly supports the TEM data on extensively dispersed nanoparticles and the explanation of the high adsorption capacity, where the homogeneous distribution results in the maximum number of active sites for complexing Pb(II). This directly demonstrates the effectiveness of liquid-assisted mechanochemical synthesis to

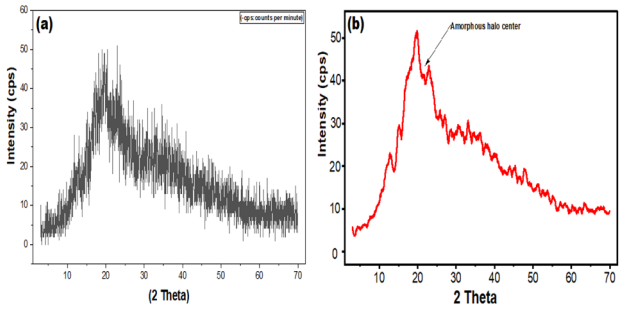

Fig. 4 Powder X-ray diffraction patterns of (a) ball-milled PKMF without Bi, showing a broad amorphous halo centred at 2θ value of ~22°, characteristic of amorphous lignocellulosic carbon, and (b) Bi-PKMF. No additional diffraction peaks are observed for Bi-PKMF, indicating that the bismuth species are amorphous and present as nanoparticles below the coherent scattering domain size (~3 nm).

achieve nanoscale doping and interfacial bonding, as proposed.[37] The combination of TEM imaging and quantitative EDX elemental mapping herein presents strong and direct proof regarding the homogeneous assembly of bismuth oxide nanoparticles in the palm kernel mesocarp fiber matrix, visually supporting the idea of functionalization and mechanochemical synthesis of homogeneous biosorbents.[23,36,38]

3.1.3 XRD results. The XRD patterns of BM-PKMF (ball-milled PKMF without bismuth) and Bi-PKMF are shown in Fig. 4a and b, respectively. Both materials exhibit a broad, diffuse scattering halo centred at $2\theta \approx 20$–$23°$, characteristic of amorphous lignocellulosic biomass and disordered carbon structures from the palm kernel mesocarp fiber matrix, as also observed by Abu Bakar (2022).[39] This confirms that the palm kernel mesocarp fiber matrix is largely non-crystalline after liquid-assisted mechanochemical processing and low-temperature thermal treatment.[40] The diffractogram highlights the amorphous halo centered at $2\theta \approx 20$–$23°$, confirming the non-crystalline nature of the carbon matrix.

Low intensity, weak, and broadened diffraction peaks may arise from trace mineral components (*i.e.*, iron or silica-containing impurities) naturally occurring in agro-waste biomass, but these reflections lack insufficient intensity and resolution to obtain any reliable quantitative phase information.[37] As a result, Rietveld refinement or percentage determination of phases was not performed. Interestingly, crystalline bismuth oxide (*e.g.*, α-Bi_2O_3 or β-Bi_2O_3) phases are not associated with any specific diffraction peaks.[40] This suggests that the bismuth species can either be amorphous or present as ultrafine nanoparticles below the XRD detection limit, as identified by the TEM micrographs, which showed their effective nanoscale dispersion in the biomass matrix. These results show that XRD is a qualitative method to confirm structural disorder and nanoscale integration, rather than for quantifying the crystalline phase.[22] This interpretation is consistent with the literature,[41] which reports that amorphous bismuth oxide (A-BiO) prepared *via* a hydrothermal method exhibits a broad featureless XRD pattern with no sharp peaks, even though bismuth is present in significant quantity.[39] In the XRD pattern of Bi-PKMF, the broad halo from the lignocellulosic matrix overlaps with and dominates the scattering from any amorphous or nanocrystalline bismuth oxide. The TEM analysis (Fig. 2) confirms the presence of 10–50 nm bismuth oxide nanoparticles, which may be polycrystalline or poorly crystalline, leading to peak broadening below the detection limit. Alternatively, the nanoparticles observed by TEM could be aggregates of even smaller crystallites. Therefore, XRD does not contradict the successful bismuth functionalisation but rather indicates that the bismuth oxide is either amorphous or nanocrystalline with very small domain sizes.

3.1.4 AFM results. AFM was employed to probe the nanoscale surface topography of pristine PKMF, ball-milled-PKMF, and Bi-PKMF over 5 μm × 5 μm scan areas (Fig. 5). The 3D topographies reveal progressive surface roughening upon ball milling and subsequent bismuth functionalisation. Pristine PKMF exhibits a relatively smooth surface, with an average roughness (R_a) of 98.4 nm and a root-mean-square roughness (R_q) of 124.7 nm. After ball milling (BM-PKMF, Fig. 5b), the surface becomes noticeably rougher (R_a = 145.2 nm and R_q = 183.5 nm) due to mechanical fragmentation and delamination of the lignocellulosic fibers.[23] Following bismuth functionalisation (Bi-PKMF, Fig. 5c), the roughness increases further (R_a = 174.3 nm and R_q = 221.6 nm), and the mean grain size decreases from 2.8 nm (pristine) to 2.1 nm (ball-milled-PKMF) and 1.6 nm (Bi-PKMF), reflecting the deposition of nanoscale bismuth oxide particles.[22]

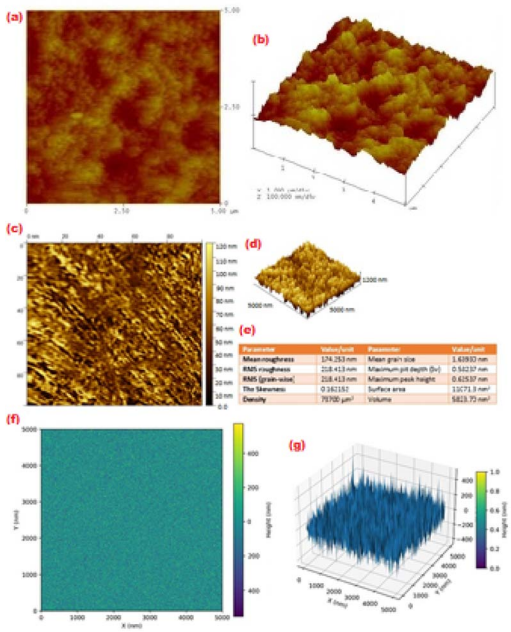

Fig. 5 Atomic force microscopy (AFM) analysis of ball-milled PKMF without bismuth, Bi-PKMF, and pristine PKMF surfaces over 5 μm × 5 μm scan areas: (a) 2D height distribution and roughness of ball milled-PKMF without bismuth, (b) 3D topography of ball-milled PKMF without bismuth, (c) 2D height distribution and roughness parameters of Bi-PKMF (R_a = 174.3 nm and R_q = 221.6 nm); (d) 3D topography of Bi-PKMF showing nanoscale surface features; (e) tabulated analytical parameters for both materials; (f) 2D height map of pristine PKMF; and (g) 3D surface reconstruction of pristine PKMF (R_a = 98.4 nm and R_q = 124.7 nm).

These results reveal a nanoscale surface topography with varying degrees of roughness.[38] The monotonic increase in surface roughness correlates with the BET surface areas (85 → 245 → 387 m^2 g^{-1}) and supports the conclusion that ball milling physically activates the fiber surface, while bismuth functionalisation introduces additional nanoscale textural features. The AFM data do not directly resolve individual cellulose microfibrils; rather, they quantify the overall nanoscale roughness that enhances the density of accessible adsorption sites.[42]

3.1.5 FTIR results. The FTIR spectrum of Bi-PKMF, as shown in Fig. 6, indicates the presence of key functional groups that are the basis of its adsorption ability. The broad band at 3282 cm^{-1} corresponds to O–H stretching of cellulose/lignin and adsorbed water, while the C=O stretching of carbonyl groups appears at 1627 cm^{-1}. The peak at 1034 cm^{-1} is attributed to polysaccharide stretching in the lignocellulosic palm kernel fiber matrix, consistent with a similar study.[40]

Importantly, the sharp peak at 534 cm^{-1} corresponds to Bi–O stretching vibrations, providing direct spectroscopic evidence for the integration of bismuth oxide (Bi_2O_3) nanoparticles into the fibrous structure. In aqueous environments, hydroxylation of these Bi–O sites produces bismuthol groups (Bi–OH), which are high-affinity binding sites for Pb(II) *via* ligand exchange and inner-sphere complexation. This represents a distinct type of active site that is not found in pure PKMF.[38]

This chemical fingerprint indicates that the material surface contains not only the inherent oxygen-containing functional groups of the biomass, but it also has newly formed bismuth-related sites.[32] These hybridized sites play a key role in enhancing the adsorption of Pb(II) ions *via* synergistic adsorption by surface complexation and ion exchange. The incorporation of bismuth generates more and highly active binding sites compared to native hydroxyl and carboxyl groups, which form the basis of palm kernel shell adsorbents and are found in other bismuth-decorated bio-sorbents that display better affinity to heavy metal cations.[22] This detailed surface chemistry correlates with the synthesis strategy and the high removal efficiency of the material for lead in contaminated water.

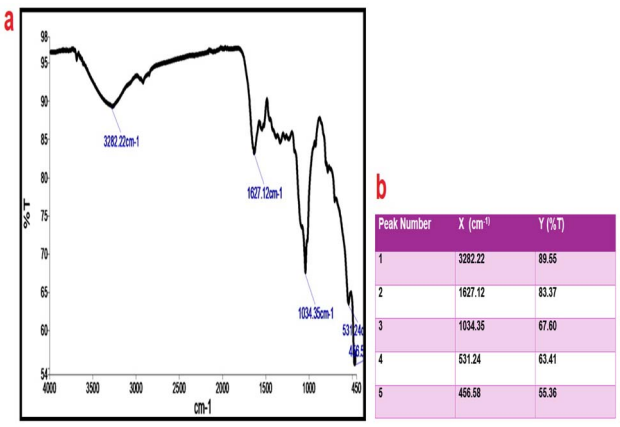

Fig. 6 (a) FTIR spectrum and (b) identification of functional groups in Bi-PKMF and confirmation of bismuth oxide integration for enhanced adsorption.

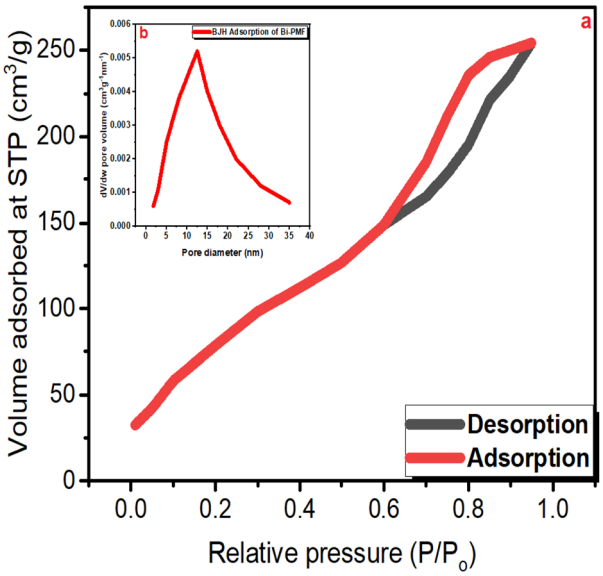

Fig. 7 BET surface area analysis of Bi-PKMF: (a) N_2 adsorption–desorption isotherms showing a Type IV mesoporous profile. (b) BJH pore size distribution indicating a primary pore diameter of ~12.5 nm.

3.1.6 BET results. The Brunauer–Emmett–Teller (BET) analysis of Bi-PKMF revealed the significant textural improvements achieved through mechanochemical synthesis. The N_2 physisorption isotherm (Fig. 7) exhibits a Type IV(a) profile with a distinct H3-type hysteresis loop in the relative pressure (P/P_0) range of 0.45 to 0.95, typical of mesoporous materials with slit-shaped pores formed by the aggregation of plate-like particles or fibrous structures. The absence of a saturation plateau at high P/P_0 and the non-closing hysteresis loop are evidence of micropores or textural porosity, which is consistent with the fibrous biomass substrate. This material exhibits a high specific surface area of 387 m^2 g^{-1} and a total pore volume of 0.068 cm^3 g^{-1}, as determined by N_2 physisorption. These values represent the mean of triplicate measurements, with standard deviations of ±15 m^2 g^{-1} and ±0.005 cm^3 g^{-1}, respectively, confirming the good reproducibility of the synthesis. The pore size distribution, calculated using the BJH method (Fig. 7b), is broad, with the highest contribution at 12.5 nm, indicating a dominant mesoporous network (2–50 nm), with significant contributions from micropores and macropores. This hierarchical porosity is directly related to the liquid-assisted grinding process, which breaks down the lignocellulosic fiber and uniformly incorporates bismuth oxide nanoparticles, creating new interfacial spaces and accessing ports.[42]

These features have direct and important implications for adsorption. Both high surface area and the mesoporous network provide a high density of available active sites, low diffusion resistance, and rapid kinetics for Pb(II) ion transport to the binding sites.[43] The excellent performance of this material can be explained by this synergistic structure with the high surface area of activated carbons and customizable functional sites of bismuth nanomaterials. It has a higher surface area than raw palm kernel shell (<100 m^2 g^{-1})[30] and is comparable to other developed bismuth-functionalized adsorbents,[32] where surface areas of 300–500 m^2

Table 3 Comparison of the performance of PKMF and Bi-PKMF

Parameter	PKMF (as-received, washed)	BM-PKMF (ball-milled only)	Bi-PKMF (ball-milled with Bi)
Surface area ($m^2\ g^{-1}$)	85 ± 8	245 ± 12	387 ± 15
Pore volume ($cm^3\ g^{-1}$)	0.021 ± 0.003	0.045 ± 0.004	0.068 ± 0.005
Pb(II) Q_0 ($mg\ g^{-1}$)	48.5 ± 2.1	78.3 ± 3.2	112.3 ± 4.1
Removal at 50 mg L^{-1} (%)	85.0 ± 1.5	91.2 ± 1.2	96.3 ± 1.1
Time to 90% removal (min)	180	120	60

g^{-1} are associated with outstanding heavy metal uptake rates. Therefore, the BET data confirm that the synthesis strategy is effective, demonstrating that Bi-PKMF is a high-surface-area, porous adsorbent, not merely surface-modified fibers.

3.1.7 Mechanochemical assessment and Bi-functionalization. To explain the individual effects of mechanical activation and chemical functionalization on the overall adsorption performance, control experiments were carried out with ball-milled palm kernel mesocarp fibers prepared under the same mechanochemical conditions, but without the bismuth precursor, namely BM-PKMF, for a direct comparison between pristine PKMF and the bismuth-decorated Bi-PKMF.

As observed in Table 3, the as-received PKMF exhibits a moderate specific surface area of 85 $m^2\ g^{-1}$ and a total pore volume of 0.021 $cm^3\ g^{-1}$, which are typical of untreated lignocellulosic biomass with low porosity and compressed fiber structure, consistent with the values in a prior study on raw palm kernel materials.[44] After ball milling, BM-PKMF exhibited an impressive 188% increase in surface area to 245 $m^2\ g^{-1}$ and an over twofold increase in pore volume to 0.045 $cm^3\ g^{-1}$, indicating that the high-energy mechanochemical process efficiently alters the hierarchical lignocellulosic architecture, exposing internal surfaces, creating new pore networks by fragmenting fibres, and delaminating them, as often seen in the literature.[31,34] This physical modification directly translated into an enhanced adsorption performance, where BM-PKMF showed a Langmuir maximum adsorption capacity of 78.3 mg g^{-1} for Pb(II), which is 61% higher than that of pristine PKMF, resulting from the increased accessibility of native oxygen-containing functional groups, including hydroxyl and carboxyl moieties exposed on the newly formed surfaces.

Interestingly, the introduction of bismuth *via* liquid-assisted grinding using bismuth nitrate and subsequent thermal crystallization produced Bi-PKMF, with further improved textural characteristics, achieving a surface area of 387 $m^2\ g^{-1}$ and pore volume of 0.068 $cm^3\ g^{-1}$. These values correspond to enhancements of 58% and 51% relative to BM-PKMF, respectively, indicating that the bismuth species present during mechanochemical processing inhibit agglomeration of the particles and pore collapse and can further increase interfacial interactions.

Importantly, the adsorption capacity of Bi-PKMF is 43% and 231% higher than that of BM-PKMF and pristine PKMF, respectively, indicating that bismuth functionalization contributes a significant chemical improvement to the physical advantages of milling. The synergistic effect of increased surface area from mechanochemical activation and the incorporation of bismuth oxide species to provide additional high-affinity binding sites through surface complexation mechanisms is responsible for the improved performance of Bi-PKMF. This is supported by the presence of Bi–O stretching vibrations at 534 cm^{-1} in its FTIR spectrum,[38] along with the homogenous dispersion of nanoscale bismuth particles observed in the TEM images and EDX elemental mapping.[37] Moreover, Bi-PKMF exhibits a kinetic advantage, with the shortest time to reach 90% removal of 60 min compared to BM-PKMF and pristine PKMF, which take 120 and 180 min, respectively. These control studies clearly demonstrate that although mechanochemical processing alone has a significant beneficial effect on the adsorptive ability of palm kernel mesocarp fiber in terms of physical activation and increased surface area, further bismuth functionalization introduces a distinct chemical contribution, resulting in a hybrid material with an overall performance unattainable by either mechanical or chemical modification alone.

3.2 Effects of adsorption parameters

3.2.1 pH effect. At low pH (≤4), most carboxylic acid groups remain protonated (–COOH), resulting in a positively charged or neutral surface that electrostatically repels Pb(II) cations and provides few available binding sites. As the pH increases to 6, the carboxylic acid groups become predominantly deprotonated ($–COO^-$) because the typical pK_a of carboxyl groups in lignocellulosic biomass is in the range of 4.0–5.0. Using the Henderson–Hasselbalch equation, at pH 6 the $[COO^-]/[COOH]$ ratio is approximately $10^{1.5} \approx 32$, corresponding to about 97% deprotonation under ideal conditions.[15] At a high pH of over 7.0, the removal is slightly reduced, likely due to precipitation effects. At all pH values, Bi-PKMF is more effective than PKMF, which is explained by the fact that bismuth oxide (Bi_2O_3) nanoparticles have more binding sites and a larger surface area, thereby augmenting uptake at neutral pH.[22] This is in line with studies demonstrating that bismuth-modified adsorbents are better at removing metals in the pH range of 6 to 7.[23] The findings indicate that pH 6 is optimal for both materials, and Bi-PKMF is more efficient and should be used in real wastewater applications.

3.2.2 Effect of dosage. As shown in Fig. 8b, the dose experiment demonstrated that Pb(II) removal is proportional to the mass of adsorbent used in both cases, plateauing at around 0.3 g as the optimum dosage, which indicates saturation of the binding sites. All doses of Bi-PKMF also exhibit a much higher removal (>90%) than PKMF (<85%), which can be attributed to its superior surface area and the existence of bismuth oxide nanoparticles that offer extra active sites for complexation.[23] The plateau indicates that beyond this dosage, additional

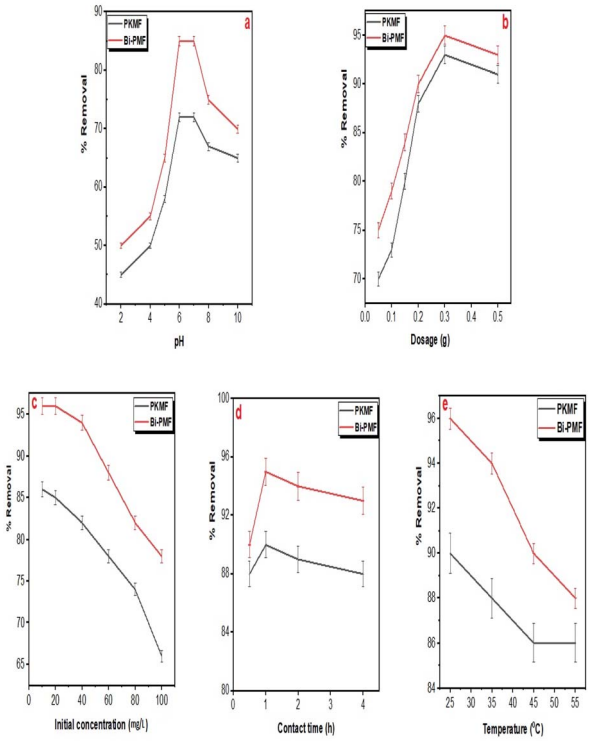

Fig. 8 Batch adsorption experiments for Bi-PKMF and PKMF. (a) Effect of pH ($C_0 = 50$ mg L^{-1}, dosage = 0.3 g, $T = 25$ °C, and $t = 2$ h); (b) effect of dosage ($C_0 = 50$ mg L^{-1}, pH 6, $T = 25$ °C, and $t = 2$ h); (c) effect of initial concentration (pH 6, dosage = 0.3 g, $T = 25$ °C, and $t = 2$ h), note that the maximum adsorption capacities (Q_0) are derived from the saturation plateau of this curve; (d) effect of contact time (C_0 = 50 mg L^{-1}, pH 6, dosage = 0.3 g, and $T = 25$ °C); and (e) effect of temperature ($C_0 = 50$ mg L^{-1}, pH 6, dosage = 0.3 g, and $t = 2$ h). All percentage lead (Pb) removals in (a), (b), (d), and (e) are at C_0 = 50 mg L^{-1}, which explains the modest 10% difference between materials under these non-saturating conditions.

increases will bring about a reduction because of overlapping active sites or aggregation, which is a widespread occurrence in porous adsorbents.[15] The high-quality performance of Bi-PKMF at low doses highlights the efficiency of this technology, thus minimizing the volume of material needed to apply this technique in practice. This is consistent with the research on bismuth-functionalized biosorbents, which show higher uptake per unit mass for modified biomass *versus* raw biomass.[22]

3.2.3 Initial concentration. According to the initial concentration study in Fig. 8c, both PKMF and Bi-PKMF display high Pb(II) removal (>90%) at low concentrations (less than 20 mg L^{-1}), which diminishes over a concentration range to about 70–85% at 100 mg L^{-1}. This tendency is inherent to adsorption saturation when the number of active sites is limited.[45] Bi-PKMF exhibited higher removal at all concentrations since bismuth oxide nanoparticles have more binding sites and greater surface area; therefore, its adsorption capacity is higher than that of pristine PKMF. This is consistent with studies on bismuth-decorated adsorbents, which show that the higher the concentration, the higher the heavy metal uptake, through optimized ion exchange and complexation.[23] The findings confirm that Bi-PKMF is superior for the removal of high-level Pb(II).

3.2.4 Contact time. The contact time study, as shown in Fig. 8d, indicates that Pb(II) adsorption by both PKMF and Bi-PKMF follows typical kinetics; during the first hour, adsorption is rapid and afterwards a slow decrease within 2–4 h. This trend is explained by the initially high number of available surface sites, which decreases as a result of site saturation and potential intra-particle diffusion.[46]

At equilibrium, Bi-PKMF (~96%) exhibits a higher percentage removal (than PKMF, at the same point, of 92%), owing to its increased surface area and the presence of numerous active sites (supplied by bismuth oxide nanoparticles), thus leading to faster and more complete adsorption. These findings validate that Bi-PKMF has greater capacity and better kinetics, making it more efficient for time-sensitive water treatment systems.[22]

3.2.5 Temperature effect. The temperature experiment showed that the Pb(II) adsorption efficiency of both PKMF and Bi-PKMF decreases slightly at temperatures between 25 °C and 55 °C, indicating an exothermic adsorption process (Fig. 8e). This suggests that Pb(II) uptake is more favorable at lower temperatures, likely because surface complexes are more stable and desorption is less favored at lower temperatures.[47] Bi-PKMF outperformed PKMF at all temperatures with higher removal percentages due to the uniform incorporation of bismuth oxides, which provide more active sites with high affinity for Pb(II) despite the changes in thermal conditions. Overall, both adsorbents exhibit an optimal performance at or near room temperature, which is beneficial for their practical and energy-efficient application in water treatment.[48]

3.3 Adsorption isotherms of PKMF and Bi-PKMF

Table 4 shows the adsorption isotherm parameters (Langmuir, Freundlich, Temkin, and Dubinin–Radushkevich (D–R)) for Pb(II) ion removal by the PKMF and Bi-PKMF adsorbents. The adsorption isotherms were constructed using the mean equilibrium uptake (q_e) from triplicate experiments at each initial concentration.

3.3.1 Langmuir isotherm. Monolayer adsorption on a uniform surface is saturated, and the Langmuir isotherm model determines the saturation at a fixed adsorption energy. The Langmuir equation can be expressed as follows:

$$q_e = \frac{Q_0 \cdot b_L \cdot C_e}{1 + b_L \cdot C_e} \quad (3)$$

where C_e is the equilibrium concentration of metal ions (mg L^{-1}), Q_0 is the monolayer adsorption capacity (mg g^{-1}), q_e is the equilibrium adsorption capacity of the adsorbent (mg g^{-1}), and b is the Langmuir binding energy constant (L mg^{-1}). Based on the equation, the slope and intercept of the C_e/q_e *vs.* C_e plot can be used to compute b and Q_0, respectively. According to the values in Table 4, the high R^2 values (>0.99) suggest monolayer adsorption on a homogeneous surface.

The higher Q_0 value for Bi-PKMF (112.3 mg g^{-1}) compared with PKMF (48.5 mg g^{-1}) indicates significantly enhanced

Table 4 Adsorption isotherm parameters for Pb(II) removal by PKMF and Bi-PKMF (experimental conditions: pH 6, $T = 25$ °C, contact time = 2 h, dosage = 0.3 g, and initial concentration range = 10–100 mg L^{-1})

Models	Parameters	PKMF	Bi-PKMF
Experimental data (at $C_0 = 100$ mg L^{-1})	C_e (mg L^{-1})	24.8	8.6
Langmuir model	Q_0 (mg g^{-1})	48.5	112.3
	b_L (L mg^{-1})	0.085	0.142
	R^2	0.992	0.998
Freundlich model	$1/n$	0.62	0.54
	k_f (mg^{-1}/n $L^{1/n}$ g^{-1})	12.8	32.5
	R^2	0.978	0.985
Temkin model	B (J mol^{-1})	985	645
	b_T (J mol^{-1})	125	198
	K_t (L g^{-1})	2.45	5.67
	R^2	0.965	0.974
Dubinin–Radushkevich model	q_D (mg g^{-1})	44.2	105.8
	E (kJ mol^{-1})	9.2	12.6
	R^2	0.960	0.970

maximum adsorption capacity due to bismuth oxide incorporation, which provides additional active sites.[22] The b_L values reflect strong affinity between Pb(II) ions and the adsorbent surfaces, with Bi-PKMF showing greater affinity. The close agreement between the Langmuir maximum capacity (Q_0) and experimental uptake at the initial highest concentration (100 mg L^{-1}) proves that the studies in the batch were under near-saturation conditions.

These results confirm the experimental layout and the credibility of the obtained Langmuir parameters. A comparison was performed to categorize the heavy metal removal capacity of the as-synthesized Bi-PKMF and PKMF in this work, as tabulated in Table 5. The comparative study in Table 5 clearly shows that the novel nanoparticle Bi-PKMF performed better, with a Pb(II) adsorption capacity of 112.3 mg g^{-1} is exceptional. This is more than twice that of the unmodified PKMF (48.5 mg g^{-1}) and is much higher than that of the previously reported palm kernel shell-derived adsorbents, including functionalized derivatives, which commonly exhibit capacities of less than 50 mg g^{-1}.

This outstanding improvement is directly linked to the novel liquid-assisted mechanochemical synthesis, which enables the molar-scale uniform integration of bismuth oxide.[27] The resulting material is a high-surface-area, multifunctional material with numerous active sites for surface complexation and ion exchange. Moreover, the enhanced adsorption capacity of the base PKMF was better than that reported in a previous study, demonstrating the efficiency of the optimized cleaning and milling protocol in maintaining[25] and accessing the native lignocellulosic structure of the fiber as a superior foundational matrix, which was further doped with bismuth.[17]

3.3.2 Freundlich isotherm. The Freundlich isotherm is used to describe adsorption on heterogeneous surfaces with nonuniform adsorption energies. The Freundlich formula is given as follows:

$$q_e = K_f \cdot C_e^{1/n} \quad (4)$$

where the constants n and K_f represent the adsorption intensity and capacity, respectively. Based on this equation, the slope and intercept of the linear relationship between $\log q_e$ and $\log C_e$ can be used to determine K_f and n. Consequently, $1/n$ values smaller than 1 indicate normal adsorption with considerable contact between the adsorbent and the metal, whereas $1/n$ values greater than one indicate cooperative adsorption. The $1/n$ values were <1 for both materials, indicating favorable adsorption. The lower $1/n$ value for Bi-PKMF (0.54) suggests a more heterogeneous surface with stronger binding sites introduced by bismuth doping. The higher K_f for Bi-PKMF (32.5) confirms its superior adsorption intensity and capacity compared with

Table 5 Comparison of maximum adsorption capacities (q_e, mg g^{-1}) of various bio-adsorbents for heavy metal removal. Values for PKMF and Bi-PKMF represent experimental equilibrium uptake at $C_0 = 100$ mg L^{-1}, pH 6, and 25 °C correspond to the Langmuir Q_0 values as saturation is approached

S/no	Adsorbate	Adsorbent	Adsorption capacity (q_e)	References
1	Pb^{2+}	Bi-PKMF	112.3 mg g^{-1}	Current study
2	Pb^{2+}	PKMF	48.50 mg g^{-1}	Current study
3	Pb^{2+}	Palm kernel shell (PKS)	49.62 mg g^{-1}	15
4	Cd^{2+}	Palm kernel shell (PKS)	42.12 mg g^{-1}	15
5	Cr^{3+}	Palm kernel shell (PKS)	49.65 mg g^{-1}	15
6	Zn^{2+}	Palm kernel shell (PKS)	41.72 mg g^{-1}	15
7	Cd^{2+}	Functionalized PKS	39.00 mg g^{-1}	14
8	Pb^{2+}	Functionalized PKS	40.00 mg g^{-1}	14
9	Zn^{2+}	Functionalized PKS	37.00 mg g^{-1}	14
10	Cr^{6+}	Functionalized PKS	40.00 mg g^{-1}	14

PKMF;[15] the higher R^2 value of Bi-PKMF also indicates a good fit to the adsorption isotherm.

3.3.3 Temkin isotherm. According to the Temkin isotherm model, it is assumed that the binding energies of adsorbents on a surface will be distributed evenly across the population. The linear equation of the Temkin equation is presented as follows:

$$q_e = \frac{RT}{b_T}\ln(K_t \cdot C_e) \quad (5)$$

where b_T (J mol^{-1}) is the Temkin constant related to the heat of adsorption, and a higher b_T indicates a steeper decrease in adsorption energy as the surface becomes more occupied. K_t (L g^{-1}) is the equilibrium binding constant at the reference adsorption heat, and a higher K_t suggests stronger binding at low coverage. R is the gas constant (8.314 J mol^{-1} K^{-1}), and T is the temperature in Kelvin. The decrease in b_T value from PKMF to Bi-PKMF implies a reduction in adsorption heat, likely due to more efficient surface coverage and interaction. The higher K_t for Bi-PKMF indicates stronger adsorbent–adsorbate interactions, consistent with the presence of bismuth-related active sites.[23]

3.3.4 Dubinin–Radushkevich (D–R) isotherm. The Dubinin–Radushkevich isotherm is typically used to describe adsorption on heterogeneous surfaces with a normal energy distribution. It is used to differentiate between chemical and physical mechanisms for the adsorption of metals. The linear D–R equation is presented in eqn (6), which is used to determine the slope and q_m from the intercept by plotting ln q_e *versus* E^2. The mean adsorption energy (E) provides information about chemical and physical adsorption.

$$\ln = q_e = \ln q_m - \beta\varepsilon^2 \quad (6)$$

The E values for PKMF (9.2 kJ mol^{-1}) and Bi-PKMF (12.6 kJ mol^{-1}) are both >8 kJ mol^{-1}, indicating that the adsorption process is governed by chemisorption.[49] This supports the findings of the Langmuir and pseudo-second-order models. The higher E value for Bi-PKMF indicates a stronger chemisorption process, which is consistent with bismuth oxide-integrated nanoparticles, enhancing surface complexation with Pb(II) ions.[38] In addition, the data for Bi-PKMF fitted the D–R isotherm better than PKMF, which agrees with the "physisorption isotherm of N_2 (Fig. 7) that has a Type IV(a) shape and distinctive H3-type hysteresis loop between the relative pressure (P/P_0) of 0.45 to 0.95, typical of mesoporous materials having slit-shaped pores being formed by aggregation of plate-like particles or fibrous structures", as confirmed in Section 3.1.6. The D–R model offers a very important understanding of the nature of the active sites. It is worth noting that the E value is 12.6 kJ mol^{-1} in the case of Bi-PKMF, indicating that the added bismuth oxide sites cause greater chemical bonding with Pb(II) and the oxygen functionalities present in the original compound. This energetic difference is evidence that the bismuth sites are not just extra surface area but are structurally different, higher-energy active sites.

Table 6 Mean adsorption kinetic parameters for Pb(II) on PKMF and Bi-PKMF adsorbents

Models	Parameters	PKMF	Bi-PKMF
Pseudo-first order	K_1 (min)$^{-1}$	0.0042	0.065
	q_e (mg g^{-1})	22.50	23.80
	R^2	0.981	0.989
Pseudo-second order	K_2 (g mg^{-1}min^{-1})	0.0028	0.0045
	q_e (mg g^{-1}) (calculated)	23.00	24.00
	q_e (mg g^{-1}) (experimental)	23.12	24.44
	R^2	0.998	0.999
Elovich model	α (mg min^{-1})	4.20	8.60
	β (g mg^{-1})	0.28	0.22
	R^2	0.963	0.972
Intra particle diffusion	K_1	1.85	2.40
	C (mg g^{-1})	5.2	8.1
	R^2	0.958	0.966

3.4 Adsorption kinetics on PKMF and Bi-PKMF

We employed four adsorption kinetic models including pseudo-first-order kinetics (Lagergren model), pseudo-second-order kinetics (Ho–McKay model), Elovich model, and intraparticle diffusion model (Weber–Morris model) to explain the adsorption mechanism of Pb(II) ions on PKMF and Bi-PKMF. Each data point in the isotherm (C_e, q_e) and kinetic (t, q_t) curves represents the mean of replicate measurements (typically $n = 3$). According to pseudo-first-order kinetics, adsorption is proportional to the amount of vacant adsorption sites, indicating that adsorption mostly occurs through physical interactions (physisorption) and that its rate is governed by mass transfer at the solid–liquid interface, and its formula is shown as follows:

$$\log(q_e - q_t) = \log q_e - (K_1/2.303)t \quad (7)$$

where K_1 is the pseudo-first-order rate constant and q_e and q_t are the equilibrium and t (minutes) adsorption capacities (mg g^{-1}), respectively. The slope and the intercept of the plot of log(q_e − q_t) *versus* (t) were used to determine the kinetic constants of the pseudo-first-order adsorption of Pb(II) on the PKMF and Bi-PKMF adsorbents (Table 6). Based on the pseudo-first-order data presented in Table 6, the greater K_1 of Bi-PKMF suggests that its adsorption kinetics is fast at the beginning owing to the availability of bismuth oxide nanoparticles, which increase the reactivity and surface accessibility.[32] A smaller qe than that obtained from the pseudo-second-order model indicates that physisorption is not the only mechanism.

The pseudo-second-order model is frequently utilized in the study of adsorption systems, in which the rate-limiting step can be chemisorption through either exchange or sharing of valence forces, such as electron sharing or exchange.[46] Hence, the exceptionally good fit of our data to this model (Table 6) is consistent with a chemisorption-mediated process.

This rate depends on the square of the number of unoccupied sites and its equation is shown in eqn (8), where K_2 is the rate constant (g mg^{-1} min^{-1}). By plotting t/q_t *vs.* time (t), with this equation, q_e and K_2 can be determined from the intercept and slope.

$$t/q_t = 1/K^2 q_e^2 + 1/q_e t \quad (8)$$

A chemisorptive mechanism is further substantiated by FTIR spectroscopy (Section 3.1.5, Fig. 6), where the decrease or shift in the BiO vibration band at approximately 534 cm^{-1} after Pb(II) adsorption suggests direct interactions between the bismuth oxide sites on the surface and the metal ions.[45,48]

Furthermore, the adsorption kinetics were investigated using the Elovich model. The Elovich model assumes that adsorption occurs on a heterogeneous surface and that the activation energy of adsorption increases exponentially with surface coverage, as is typical of chemisorption on non-uniform sites of varying energy, as expressed in eqn (9). In this model, α is the initial adsorption rate and β is the adsorption coefficient, and the plot of q_t *vs.* ln (t) is used to determine the constants α and β, as shown in Table 6.

$$q_t = 1/\beta \ln[\alpha\beta] + 1/\beta \ln t \quad (9)$$

The higher α for Bi-PKMF reflects a higher initial adsorption rate than PKMF, while the lower β suggests a more heterogeneous surface with abundant active sites due to bismuth incorporation.[32]

To characterize solute transfer in solid–liquid adsorption, intraparticle diffusion was implemented to determine the adsorption mechanism. The intraparticle diffusion Weber–Morris model assumes that adsorption is controlled, at least in part, by diffusion of adsorbate molecules within the pores of the adsorbent rather than solely by surface reactions. The theoretical equation is given in eqn (10).

$$q_t = K_{id} t_2^{1} + C \quad (10)$$

where K_{id} (mg g^{-1} $min^{-1/2}$) is the intraparticle diffusion rate constant, and C (mg g^{-1}) is the boundary layer effect and thickness. Likewise, the slope and intercept of the linear plot of q_t *vs.* $t^{1/2}$ were used to obtain K_{id} and C. Based on these calculations, it can be seen in Table 6 that the higher K_{id} for Bi-PKMF results in quicker diffusion of Pb(II) into its mesoporous structure (which is demonstrated by the BET analysis). The increased C value indicates that surface adsorption and boundary layer effects play a more significant role, which is consistent with the increased surface area and functionalization.[6]

In brief, the high rate of Pb(II) adsorption by Bi-PKMF (90% in 60 min) and its Dubinin–Radushkevich adsorption energy of 12.6 kJ mol^{-1} offer a seemingly paradoxical situation as chemisorption is expected to occur more slowly when diffusion is the rate-limiting step. This inconsistency is resolved by the mesoporous architecture of the material. The BET analysis showed a pore size of 12.5 nm (Section 3.1.6), which can easily accommodate hydrated Pb(II) ions ($\approx$0.4–0.5 nm) with very low steric hindrance. As a result, the resistance to intraparticle diffusion is greatly reduced, including a high Weber–Morris intraparticle diffusion rate constant (K_{id} = 2.40 mg g^{-1} $min^{-1/2}$, Table 6). The diffusion barrier has been eliminated, and the rate-limiting step is now the surface chemisorption reaction at the numerous abundant Bi–O and $-COO^-$ sites. This is exactly the case with the pseudo-second-order kinetic model ($R^2 > 0.999$), where the adsorption rate is determined by the square of the concentration of unoccupied sites, a rate law that is surface reaction-controlled. Therefore, the combination of chemical affinity (large E value) and physical accessibility (mesoporous structure) helps in understanding the strength and rate of Pb(II) sequestration by Bi-PKMF.

3.5 Thermodynamics of adsorption

Entropy (ΔS^0), free energy (ΔG^0), and enthalpy (ΔH^0) are important thermodynamic parameters. The thermodynamics of Pb(II) adsorption on PKMF and Bi-PKMF were evaluated at different temperatures (298.15 K, 308.15 K, 318.15 K and 328.15 K) using the following equation:

$$\ln K = \frac{\Delta S^\circ}{R} - \frac{\Delta H^\circ}{RT} \quad (11)$$

where R and T are the gas constant (8.314 J mol^{-1} K^{-1}) and temperature (K), respectively, and the van't Hoff equation was plotted as $1/T$ *vs.* ln K^{-1}. The free energy of specific adsorption, ΔG^0 (kJ mol^{-1}), was calculated using the following equation:

$$\Delta G^\circ = \Delta H^\circ - T\Delta S^\circ \quad (12)$$

Negative $\Delta G°$ values at all temperatures in Table 7 confirm that the adsorption of Pb(II) on PKMF and Bi-PKMF is spontaneous. The decrease in the $\Delta G°$ value with increasing temperature indicates reduced spontaneity at higher temperatures, consistent with the observed decrease in removal efficiency. The negative $\Delta H°$ value confirms that it is an exothermic adsorption

Table 7 Pb(II) adsorption thermodynamic parameters for PKMF and Bi-PKMF

Adsorbent	T (K) = T (°C) + 273.15	K^{-1} (L g^{-1})	$\Delta G°$ (kJmol^{-1})	$\Delta H°$ (kJmol^{-1})	$\Delta S°$ (J mol^{-1} K^{-1})	R^2
PKMF	25	5.75	−4.33	−19.01	−49.32	0.991
PKMF	35	4.50	−3.86	−19.01	−49.32	0.991
PKMF	45	3.35	−3.20	−19.01	−49.32	0.991
PKMF	55	2.83	−2.84	−19.01	−49.32	0.991
Bi-PKMF	25	12.00	−6.16	−29.02	−77.07	0.987
Bi-PKMF	35	7.83	−5.27	−29.02	−77.07	0.987
Bi-PKMF	45	5.06	−4.29	−29.02	−77.07	0.987
Bi-PKMF	55	4.05	−3.81	−29.02	−77.07	0.987

reaction, where stronger adsorption occurs at lower temperatures. The more negative values of ΔH for Bi-PKMF indicate a higher binding energy associated with bismuth oxide nanoparticles, which provide more active sites to participate in surface complexation and ion exchange. The $-\Delta S^{\circ}$ value indicates that the randomness at the solid–liquid interface decreases in the process of adsorption, since the Pb(II) ions are bound to the adsorbent surface. The larger negative $-\Delta S^{\circ}$ value of Bi-PKMF (-77.07 J mol^{-1} K^{-1}) than that of PKMF (-49.32 J mol^{-1} K^{-1}) suggest an ordered adsorption process, probably because of the organized nanoscale structure and enhanced site heterogeneity arising from bismuth doping. These thermodynamic findings verify the strong performance of Bi-PKMF for the remediation of Pb(II)-contaminated water at low temperatures, supporting its practical usability and economic viability.

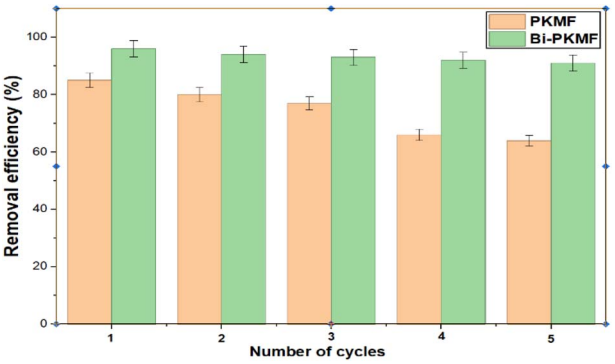

Fig. 9 Reusability of PKMF and Bi-PKMF for Pb(II) adsorption over five consecutive adsorption–desorption cycles. Adsorption conditions: 50 mL of 50 mg L^{-1} Pb(II), 0.3 g of adsorbent, pH 6, 2 h, and 25 °C. Regeneration: 0.1 M HNO_3 and 4 h.

3.6 Desorption and regeneration studies

To evaluate the practical reusability and economic viability of the synthesized adsorbent, desorption and multi-cycle regeneration experiments were conducted.

3.6.1 Adsorbent loading. Firstly, batch adsorption experiments were conducted to load the adsorbents with Pb(II). An appropriate amount of PKMF or Bi-PKMF (0.3 g, the optimal dosage) was added to 50 mL of 50 mg L^{-1} Pb(II) solution at a pH of 6. At 25 °C, the mixture was stirred at 150 rpm for 2 h (established equilibrium time). The loaded adsorbent was then separated by vacuum filtration, washed lightly with a small amount of DI water to remove the free ions, and dried at 60 °C.

3.6.2 Preliminary desorption screening. In this step, Pb-loaded Bi-PKMF was subjected to the influence of four eluents (0.1 M each): hydrochloric acid (HCl), nitric acid (HNO_3), acetic acid (CH_3COOH), and ethylenediaminetetraacetic acid disodium salt (Na_2-EDTA). The eluent (20 mL) solution was contacted with the adsorbent (0.1 g) and shaken for 4 h. The concentration of Pb(II) desorbed in the supernatant was determined to calculate the desorption efficiency (%). During multi-cycle regeneration, the results of the screening indicated that 0.1 M HNO_3 was the best eluent for use in the regeneration study. Four successive adsorption–desorption cycles were carried out. The conditions for each cycle are as follows:

- Adsorption: 50 mL of 50 mg L^{-1} Pb(II) at pH 6 was treated with 0.3 g of adsorbent for 2 h.
- Separation washing: The adsorbent was dried, rinsed using DI water, and filtered.
- Desorption/regeneration: 50 mL of 0.1 M HNO_3 was stirred with the loaded adsorbent for 4 h.
- Recovery and neutralization: The regenerated adsorbent was filtered, flushed with DI water until the filtrate became neutral pH (~6), and dried overnight at 60 °C. The efficiency of Pb(II) removal% per adsorption cycle was calculated and compared. The control experiment involved a parallel experiment with DI water as a desorption agent.

3.7 Regeneration and reusability studies

The usefulness of an adsorbent is not limited to its original capacity but also its regenerability. The screening of the eluent showed that acidic and chelating agents were effective for desorbing Pb(II) from Bi-PKMF. The desorption efficiencies were evaluated with 0.1 M HNO_3 (92.5%), 0.1 M HCl (88.1%), 0.1 M Na_2-EDTA (81.7%), and 0.1 M CH^3COOH (65.3%). The superior performance of HNO_3 could be explained by its high ionic strength and capacity to protonate the active sites on the adsorbent (*e.g.*, Bi–O and –COO–), reversing the surface complexation and ion exchange interactions between Pb(II) and the adsorbent. The DI water control had negligible desorption (≤5%), which proved that the binding was strong and non-physical. All regeneration experiments were conducted in triplicate to ensure statistical reliability, and the results are presented as the mean ± standard deviation (Fig. 9). The amount of Pb(II) adsorbed (q, mg g^{-1}) was determined at the end of each cycle to measure the capacity retention in excess of percentage removal. Pristine PKMF exhibited a gradual decrease in adsorption capacity, with a value in cycle 1 of 7.09 ± 0.15 mg g^{-1}, which decreased to 5.71 ± 0.23 mg g^{-1} in cycle 5, indicating a 19.5% loss and cumulative degradation and irreversible binding of the sites. The increase in standard deviation (between ± 0.15 to ± 0.23) indicates the increasing heterogeneity of the material performance in terms of lignocellulosic matrix degradation, probably because of the uneven lignocellulosic matrix degradation over time as a result of repeated exposure to acid. Conversely, Bi-PKMF exhibited a significantly more stable performance, and its capacity only declined from 7.51 ± 0.14 mg g^{-1} to 8.03 0.10 mg g^{-1} throughout the five cycles, just a 6.5% change. The standard deviations (±0.10–0.14) are low, which indicates the synthesis reproducibility and the strength of the bismuth-functionalized material. The high capacity retention of Bi-PKMF is attributed to the fact that bismuth oxide nanoparticles are anchored on the fiber matrix, which prevents their leaching in acids and preserves the lignocellulosic structure beneath them. These results indicate that Bi-PKMF is not only a high-capacity adsorbent but also a highly regenerable and durable material that can be used in real water treatment. The findings verify that Bi-PKMF is not only a high-capacity adsorbent but also a robust and recyclable

adsorbent, which is essential in cost-effective and sustainable water treatment processes.

3.8 Proposed mechanism of adsorption

There are two sources of active sites in Bi-PKMF, the palm kernel mesocarp fiber lignocellulosic matrix and the incorporated bismuth oxide nanoparticles, as shown in Fig. 10. Fourier transform infrared (FTIR) spectroscopy gives direct evidence of these features. The broad band at 3282 cm^{-1} corresponds to the O–H stretching band of the alcoholic and phenolic hydroxyl groups of cellulose and lignin. These hydroxyl groups can engage in metal binding by proton exchange and the formation of monodentate or bidentate surface complexes. The peak at 1627 cm^{-1} is attributed to the carbonyl stretching, which is mainly caused by carboxylic acid groups.

The carboxylic acid moieties (–COOH) in lignocellulosic materials typically have pKa values in the range of 4.0–5.0. At the working pH of 6, these groups are predominantly, but not completely, deprotonated to form carboxylate anions ($–COO^-$). The partially deprotonated surface provides negatively charged sites that can electrostatically attract cationic Pb(II) ions and participate in chelation. Additionally, the remaining protonated –COOH groups can engage in hydrogen bonding or ligand exchange with Pb(II) after deprotonation induced by metal binding. Thus, the adsorption mechanism involves dynamic equilibrium between protonated and deprotonated forms rather than a single fully deprotonated state.

This assignment is directly supported by the pH-dependent adsorption profile (Fig. 8a), where the removal efficiency is low when conditions are highly acidic, and when the conditions are not acidic but deprotonation is preferential (*i.e.*, at pH 6). Most importantly, the broad peak at 534 cm^{-1} in the spectrum of Bi-PKMF is associated with Bi–O stretching vibrations, which is clear spectroscopic evidence of the incorporation of bismuth oxide. These Bi–O sites are surface-hydroxylated to bismuthol groups (Bi–OH) in aqueous environments, which are a unique and high-affinity class of binding sites lacking in the pristine PKMF. These bismuthol complexes are capable of ligand–exchange reactions with Pb(II) ions to produce inner-sphere surface complexes of the form ≡Bi–O–Pb or $(\equiv Bi–O)_2$–Pb, which are stronger covalently directed than the interactions of the native oxygen functionalities alone. The predominant role of surface chemistry or physical structure in the process of metal adsorption can now be resolved quantitatively using experimental data. The mean free energy of adsorption (E) is the quantity obtained from the Dubinin–Radushkevich (D–R) isotherm model, which represents the difference between physical and chemical sorption. In the case of pristine PKMF, the E value of 9.2 kJ mol^{-1} is greater than the set limit of 8 kJ mol^{-1}, and thus, chemisorption prevails. Upon bismuth functionalization, the E value significantly increases to 12.6 kJ mol^{-1}. This increase is not just incremental but reflects a qualitatively stronger chemical interaction, which can be directly attributed to the greater bond energy in Pb(II) complexation at the Bi–O positions than in natural oxygen groups. The doubling of the maximum adsorption capacity (from 48.5 to 112.3 mg g^{-1}) cannot be attributed solely to the effect of surface area, but instead suggests some new, stronger binding processes. In addition, the pseudo-second-order kinetic model, which shows excellent agreement with the experimental data with correlation coefficients greater than 0.999, is fundamentally based on the assumption that the rate-limiting step involves chemisorption through valence forces *via* electron sharing or exchange.

All these pieces of evidence together prove that the determining factor in Pb(II) uptake is surface chemistry. Nevertheless, the outstanding physical characteristics of Bi-PKMF cannot be neglected. BET analysis confirmed a high specific surface area of 387 m^2 g^{-1}, and the well-developed mesoporous network with the major pore diameter of 12.5 nm plays an indispensable role. The large surface area serves as an amplifier to maximize the concentration of accessible active sites per unit mass of adsorbent, while the mesoporous architecture reduces the diffusion barriers and provides speedy routes for the transport of Pb(II) ions to the internal binding sites. In the absence of a high surface area, most of the chemical sites would be buried and inaccessible; conversely, without chemical sites, the surface would bind metals with only moderate, non-specific affinity *via* physisorption. Thus, the overall adsorption process on Bi-PKMF can be described as a multi-step process that combines both physical transport and chemical binding.

Initially, the diffusion of Pb(II) ions to the surface of the adsorbent occurs *via* film diffusion, which is aided by the large surface area and the good concentration gradient that causes the movement. The ions then gradually enter the interior of the adsorbent particles *via* the mesopore network, in which the pore size of probably 12.5 nm is large enough to allow access to all the active sites within the material without significant steric hindrance. Upon approaching the vicinity of a binding site, the prevailing retention process is determined by the local surface functionality. On the surface of bismuth oxide, the surface-hydroxylated Bi–OH groups participate in ligand exchange with

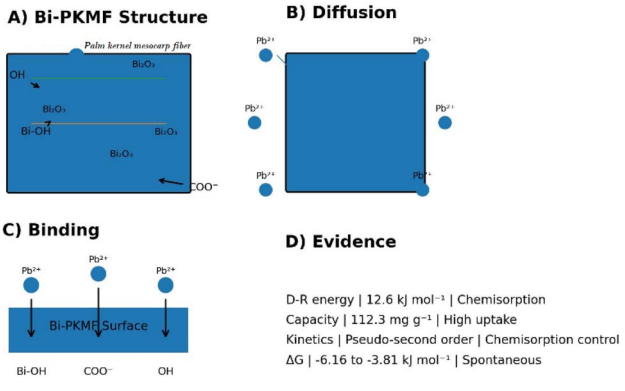

Fig. 10 Proposed Pb(II) adsorption mechanism on Bi-PKMF. (A) Active sites: Bi–OH (from Bi_2O_3), $–COO^-$, and –OH on the fiber matrix. (B) Pb^{2+} ions diffuse through the mesoporous network. (C) Binding *via* inner-sphere complexation (Bi–OH), electrostatic attraction/chelation ($–COO^-$), and coordination (–OH). (D) Key evidence: D–R energy (12.6 kJ mol^{-1}, chemisorption), high capacity (112.3 mg g^{-1}), pseudo-second-order kinetics, and negative ΔG (spontaneous).

Pb(II), releasing protons and forming stable inner-sphere complexes. This is the most energetically favourable and strongest interaction, which is consistent with the high D–R adsorption energy and the exothermic enthalpy change of −29.02 kJ mol^{-1}. Simultaneously, at the carboxylate sites, the negatively charged –COO$^-$ groups will electrostatically attract Pb(II) cations and may form chelate rings *via* coordination with the metal centre. The hydroxyl groups are involved in proton exchange of and the formation of weaker coordinate bonds. It is important to note that at the optimal pH of 6, carboxylic acid groups are predominantly deprotonated (approximately 97% based on an assumed pKa of 4.5), but some protonated –COOH sites remain and may also contribute to Pb(II) binding *via* hydrogen bonding or ligand exchange. The net reaction is spontaneous, as demonstrated by the negative Gibbs free energy values (between −6.16 and −3.81 kJ mol^{-1}), and entails a change in entropy (−77.07 J mol^{-1}K^{-1}), which represents the arrangement of hydrated Pb(II) ions into regular surface complexes.

The basis of this mechanistic system is the spectroscopic identification of active sites, quantitative energy estimation based on isotherm modeling, and kinetic analysis of the rate-determining steps, which fully explain the high adsorption activity of Bi-PKMF and provide a rational background for the use of this system in the purification of lead-contaminated water.

3.9 Study implications and limitations

3.9.1 Environmental and economic implications. The synthesis of Bi-PKMF through liquid-assisted grinding offers immense environmental and economic benefits. On the environmental side, it aligns with a circular economy model, as palm kernel mesocarp fiber (PKMF), an agricultural by-product, is employed as a high-value remediation material. This will result in less waste disposal and emissions from open burning. The synthesis is also green technology, which does not consume as much solvent and energy as that in the traditional hydrothermal or sol–gel processes. Economically, the utilization of abundant, low-cost PKMF and scalable mechanochemical route is a potential avenue to set up large-scale adsorbent manufacturing. The high reusability of Bi-PKMF (>90% capacity retained after 5 cycles) directly reduces operation costs and secondary waste generation in water treatment processes, making it economically viable and practical for the mitigation of lead pollution.

3.9.2 Limitations and required future investigations. Although the combined results of these experiments are strong evidence that a chemisorption process is occurring involving surface complexation with oxygen-containing functional groups and bismuth oxide sites, the consistent assignment of the mechanistic data in this initial experiment cannot be done without direct spectroscopic evidence. The interpretation provided in the proposed mechanism is primarily based on macroscopic observations, including FTIR identification of possible binding sites, pH-dependent uptake kinetics, pseudo-second-order kinetics, Dubinin–Radushkevich adsorption energies above the chemisorption threshold, and thermodynamic parameters that indicate the formation of ordered surface complexes. The combination of these various results suggests that the mechanism is predominantly controlled by chemical bonding rather than physical adsorption, but they do not provide direct evidence of the particular complex formed on the surface. This requires several characterization method to elucidate the final mechanistic explanation, which is only hinted at in the current work. Analysis of the Pb 4f binding energies, before and after adsorption, and X-ray photoelectron spectroscopy analysis of the chemical state of adsorbed lead would confirm the state of the adsorbed lead and allow the discrimination among the following mechanisms of adsorption: precipitation, electrostatic attraction, and inner-sphere complexation. EXAFS spectroscopy would provide quantitative bond distances and coordination numbers, showing whether Pb(II) will be inner-sphere bound to the Bi–O and –COO$^-$ sites or outer-sphere and hydrated species. Direct measurement of zeta potential values over the pH gradient would directly determine the point of zero charge and confirm the electrostatic contribution to uptake by comparing the surface charge with the measured profile of pH-edges.

Additional desorption experiments using selective eluents would differentiate reversible and irreversible bound fractions of lead in the ion-exchangeable and irreversible complexes, respectively, which would further limit the binding mechanism. These sophisticated spectroscopic and surface characterization studies will be done in future research to propose the final mechanistic explanation, whereas the present research can make conjectures only depending on the experimental evidence.

4 Conclusion

A novel bismuth-decorated palm kernel mesocarp fiber (Bi-PKMF) was successfully produced through green mechanochemical-thermal processing. Extensive characterization (SEM-EDX, TEM, BET, and FTIR) revealed the uniform dispersion of bismuth oxide nanoparticles in the lignocellulosic matrix to form a high-surface-area mesoporous material (387 m^2 g^{-1} and pore size of 12.5 nm). Neutral control experiments with ball-milled PKMF (BM-PKMF) showed that bismuth functionalization is not a replication of the physical advantages of mechanical activation. Bi-PKMF showed superior Pb(II) adsorption capacity (112.3 mg g^{-1}), which is 231% higher than that of pristine PKMF (48.5 mg g^{-1}), and more than 90% removal was observed in 60 min at pH 6. The pseudo-second-order model and kinetic data fit (R^2 > 0.999) and the Dubinin-Radushkevich adsorption energy (12.6 kJ mol^{-1}) proved chemisorption as the dominant process. Bi-PKMF has a mesoporous structure that reduces the resistance to intraparticle diffusion, which enables rapid access to the active sites (Bi–O, –OH, and –COO$^-$). The change in thermodynamic parameters was spontaneous (ΔG^0 < 0), exothermic (ΔH^0 = −29.02 kJ mol^{-1}), with ordered adsorption. Bi-PKMF has very high reusability, retaining more than 90% of its original capacity after 5 regeneration cycles. This study confirms that Bi-PKMF is a high-performing, sustainable biosorbent for remediating lead, showing that surface chemistry, rather than physical structure, is the critical element in the uptake of metals.

Author contributions

Amarachi Udoka Nkwoada: conceptualization, methodology, formal analysis, investigation, writing – original draft, project administration, funding acquisition. Simeon Chukwudozie Nwanonenyi: validation, resources, writing – review & editing, supervision. Callistus Izunna Iheme: data curation, investigation, writing – review & editing, visualization. Ali Bilar: validation, investigation, formal analysis, writing – review & editing. Ijeoma Akunna Duru: methodology, investigation, data curation. Tochukwu Ifeanyi Nwakile: resources, validation, writing – review & editing. Divinefavour Anioke: methodology, investigation, and formal analysis. Janefrances Oluebube Onwuemeodo: methodology, investigation, and formal analysis. Chukwuemeka Fortunatus Nnadozie: investigation, data curation, validation. Celestine Chidubem Chukwunonyerem: software, formal analysis, visualization. Favour Ogadinma Izuagba: methodology, investigation. Uchenna Gift Nwaneri: writing – review & editing, project administration, supervision.

Conflicts of interest

There are no conflicts to declare.

Data availability

Data availability will be made available on reasonable request.

References

1 P. Zhang, M. Yang, J. Lan, Y. Huang, J. Zhang, S. Huang, Y. Yang and J. Ru, *Toxics*, 2023, **11**, 828.
2 O. Azubuike, A. Basil, N. Amarachi, E. Uchechi, B. Ali and O. Cynthia, *Water, Air, Soil Pollut.*, 2025, **236**, 773.
3 M. Meena, P. Sonigra and G. Yadav, *Environ. Sci. Pollut. Res.*, 2021, **28**, 2485–2508.
4 A. U. Nkwoada, I. C. Iwu, S. A. Kalu, C. A. Nweze and B. N. Anukam, *Phys. Chem. Res.*, 2025, **13**, 129–138.
5 P. Elechi, A. U. Nkwoada, C. S. Okpara, T. I. Nwakile, D. P. Fapojuwo, C. P. Chikezie, S. A. Kalu, C. I. Iheme, C. A. Nweze, S. C. Ukanero, C. K. Oguzie and C. I.-A. Nwoko, *Next Mater.*, 2026, **11**, 101581.
6 Z. Saddique, M. Imran, A. Javaid, S. Latif, T. H. Kim, M. Janczarek, M. Bilal and T. Jesionowski, *Environ. Res.*, 2023, **229**, 115861.
7 J. Idris, S. Osman, E. Gaius and C. Christian, *Environ. Eng. Manag. J.*, 2017, **16**, 26–57.
8 D. A. Axelrad, E. Coffman, E. F. Kirrane and H. Klemick, *Environ. Int.*, 2022, **169**, 107475.
9 A. Carocci, A. Catalano, G. Lauria, M. S. Sinicropi and G. Genchi*Food Toxicology*, ed. P. de Voogt and F. A. Gunther, Springer International Publishing, Cham, 2016, pp. 45–67.
10 S. Collin, A. Baskar, D. M. Geevarghese, M. N. V. S. Ali, P. Bahubali, R. Choudhary, V. Lvov, G. I. Tovar, F. Senatov, S. Koppala and S. Swamiappan, *J. Hazard. Mater. Lett.*, 2022, **3**, 100064.
11 P. Mishra, S. Ali, R. Kumar, S. Shekhar and J. Trace, *Elem. Miner.*, 2025, **14**, 100259.
12 O. B. Abogunrin-Olafisoye, O. Adeyi, A. J. Adeyi and E. O. Oke, *Waste Manag. Bull.*, 2024, **2**, 214–228.
13 I. Uchegbulam, E. O. Momoh and S. A. Agan, *Clean. Mater.*, 2022, **6**, 100154.
14 R. Baby, M. Z. Hussein, Z. Zainal and A. H. Abdullah, *J. Hazard. Mater. Adv.*, 2023, **10**, 100253.
15 R. Baby, B. Saifullah and M. Z. Hussein, *Sci. Rep.*, 2019, **9**, 18955.
16 B. Osei Bonsu, M. Takase and J. Mantey, *Heliyon*, 2020, **6**, e05266.
17 C. Marcuello, B. Chabbert, F. Berzin, N. B. Bercu, M. Molinari and V. Aguié-Béghin, *Materials (Basel)*, 2023, **16**, 2440.
18 E. O. Babatunde, S. Enomah, O. M. Akwenuke, M. A. Ibeh, C. O. Okwelum, M. M. Mundu, P. O. Adepoju, A. O. Aki, O. D. Oghenejabor, T. F. Adepoju, C. O. Ifedora and K. Mabel, *South African J. Chem. Eng.*, 2025, **52**, 200–210.
19 M. S. M. Zaini, M. Arshad and S. S. A. Syed-Hassan, *J. Bioresour. Bioprod.*, 2023, **8**, 66–77.
20 C. L. Lee, P. S. H'ng, M. T. Paridah, K. L. Chin, U. Rashid, M. Maminski, W. Z. Go, R. A. R. Nazrin, S. N. A. Rosli and P. S. Khoo, *R. Soc. Open Sci.*, 2018, **5**, 180775.
21 J. Liu, S. Du, Q. Zhu, A. Labidi, H. Wang and C. Wang, *J. Environ. Chem. Eng.*, 2024, **12**, 114790.
22 S. Jiang, Y. Zhang and J. Gong, *Environ. Sci. Nano*, 2024, **11**, 1332–1367.
23 J. Liao, X. He, Y. Zhang, W. Zhu, L. Zhang and Z. He, *Sci. Total Environ.*, 2022, **819**, 153145.
24 K. H. Thamir, H. A. Ahmed, S. Z. Al-Ashoor, P. Kanjariya, M. Akku, R. Thakur, G. D. A. Jebaselvi, S. Choudhury, M. A. Rusho and H. M. Alkahtani, *J. Inorg. Organomet. Polym. Mater.*, 2025, **35**, 8249–8267.
25 W. A. Ali, S. E. Richards and R. H. Alzard, *J. Ind. Eng. Chem.*, 2025, **149**, 63–93.
26 C. Zhao, L. Xiao, Z. Chen and Y. Zhang, *Accounts Mater. Res.*, 2024, **5**, 1583–1597.
27 J. Choma, B. Szczęśniak and M. Jaroniec, *Molecules*, 2025, **30**, 3125.
28 R. Singh and R. Bhateria, *ACS Omega*, 2020, **5**, 10826–10837.
29 A. R. Katte, J. Mwero, M. Gibigaye and D. O. Koteng, *Results Eng*, 2023, **17**, 100903.
30 K. S. Ukanwa, K. Patchigolla, R. Sakrabani and E. Anthony, *Molecules*, 2020, **25**, DOI: 10.3390/molecules25215028.
31 J.-L. Do and T. Friščić, *ACS Cent. Sci.*, 2017, **3**, 13–19.
32 H. Yan, X. Jiang, H. Xia, L. Zhang, Q. Zhang, W. Zhang, C. Xin and K. Zeng, *Desalin. Water Treat.*, 2021, **230**, 372–383.
33 J. Han, J. Shao, X. He, N. Li, Y. Qian, D. Chen and J. Lu, *J. Environ. Chem. Eng.*, 2025, **13**, 116485.
34 D. Szczerba, J.-L. Do, D. Tan, H. M. Titi, N. Geoffroy, M. del C. M. de Lucas, J. Boudon, I. Halasz, T. Friščić and S. A. J. Kimber, *RSC Mechanochemistry*, 2024, **1**, 255–262.
35 H. Arshad, M. U. Tahir, F. Rehman, L. Wang, J. Wang, X. Su and C. Yang, *Appl. Surf. Sci.*, 2022, **574**, 151678.

36 C. Gomez, G. Hallot and M. Port, S. N. Grumezescu, *Inorganic Frameworks as Smart Nanomedicines*, William Andrew Publishing, 2018, pp. 449–487.
37 C. Wang, H. Hu, M. Chen, Q. Wang, C. Liu, M. Chen, S. Yan and Q. Zhang, *J. Clean. Prod.*, 2022, **340**, 130747.
38 M. Prakash, H. P. Kavitha, S. Abinaya, J. P. Vennila and D. Lohita, *Sustain. Chem. Pharm.*, 2022, **25**, 100547.
39 N. F. Abu Bakar, N. Abd Rahman, M. B. Mahadi, S. A. Mohd Zuki, K. N. Mohd Amin, M. Z. Wahab and I. Wuled Lenggoro, *Mater. Today Proc.*, 2022, **48**, 1899–1904.
40 G. N. Sambo, A. O. Adeola and S. A. Muhammad, *Appl. Water Sci.*, 2024, **14**, 113.
41 X. Li, Y. Sun, T. Xiong, G. Jiang, Y. Zhang, Z. Wu and F. Dong, *J. Catal.*, 2017, **352**, 102–112.
42 P. Ying, J. Yu and W. Su, *Adv. Synth. Catal.*, 2021, **363**, 1246–1271.
43 R. J. Allenbaugh and A. Shaw, *Results Chem.*, 2023, **5**, 100827.
44 P. W. Huisken Mejouyo, E. M. Tiaya, N. R. Sikame Tagne, S. T. Tiwa and E. Njeugna, *Results Mater*, 2022, **14**, 100284.
45 B. Haider, M. Imran, A. Naeem, H. S. El-Beltagi, H. Arshad, A. Hussain, U. Zulfiqar, N. Y. Rebouh, P. V. V. Prasad and I. Djalovic, *Sci. Rep.*, 2025, **15**, 22823.
46 S. Mohamed Nasser, M. Abbas and M. Trari, *Prog. React. Kinet. Mech.*, 2024, **49**, 14686783241226858.
47 Sheetal and J. Pal, *Environ. Monit. Assess.*, 2024, **196**, 570.
48 J. M. Jose, E. H. E. Gladis and J. J, *ECS Trans.*, 2022, **107**, 18753.
49 K. Y. Foo and B. H. Hameed, *Chem. Eng. J.*, 2010, **156**, 2–10.